Journal of Electron Spectroscopy and Related Phenomena 195 (2014) 409–422

Contents lists available at ScienceDirect

Journal of Electron Spectroscopy and Related Phenomena

journal homepage: www.elsevier.com/locate/elspec

Some future perspectives in soft- and hard- X-ray photoemission☆

Charles S. Fadley[a,b,*], Slavomir Nemšák[a,b]

[a] Department of Physics, University of California Davis, Davis, CA 95616, USA
[b] Materials Sciences Division, Lawrence Berkeley National Laboratory, Berkeley, CA 94720, USA

ARTICLE INFO

Article history:
Received 18 April 2014
Received in revised form 21 May 2014
Accepted 5 June 2014
Available online 9 July 2014

Keywords:
Photoemission
X-ray photoemission
Hard X-ray photoemission
Photoelectron diffraction
Hard X-ray photoelectron diffraction
Photoelectron holography
Ambient pressure photoemission
Angle-resolved photoemission
ARPES
HARPES
XPS
XPD
HXPD
HXPS
HAXPES
PH
Standing wave photoemission
Synchrotron radiation
Spintronics

ABSTRACT

We discuss several recent developments in photoemission, with comments on their perspectives for the future. These include an adequate allowance for differential cross section effects in core- and valence-angular distributions, as well as more accurate one-step modeling of angle-resolved photoemission (ARPES); the use of higher photon energies from the soft- to hard- X-ray regime to permit probing bulk electronic structure and buried layers and interfaces; extending ARPES into the soft- and hard- X-ray regimes; tailoring the X-ray wave field through X-ray optical effects including standing waves, total reflection, and tuning through resonances; using standing-wave excitation to provide much enhanced depth sensitivity in studying solid/gas and solid/liquid interfaces; and applying photoelectron holography to time-resolved studies of molecular reactions and dissociation. Specific application examples include a magnetic semiconductor, multilayer structures of complex metal oxides, a thin water solution on a metal oxide surface, and a halo-substituted benzene molecule.

1. Introduction

We will in this article discuss a few recent developments in soft- and hard- X-ray photoemission that relate to the overall topic of this issue: structure determination and wave-function analysis, with special emphasis on the future perspectives that these suggest. Structure determination will be considered both from the point of view of using (SW) standing-wave excitation, together with other X-ray optical effects and total reflection, in studies of multilayer solid samples, but also at the atomic level from the point of view of photoelectron diffraction (PD) and holography (PH), including potential time-resolved studies with free-electron lasers. Wave-function analysis will be discussed in the context of angle-resolved photoemission (ARPES) using higher-energy soft and hard X-ray excitation so as to probe more deeply into materials.

We begin by introducing some of the basic parameters of the photoemission process related to these developments, and then consider more specific topics and applications. We will also point in several places in this article to discussions by other authors in this issue, so as to be complementary, but not repetitive, to them. For example, Gray [1] has written an excellent article on standing-wave effects whose contents we will not repeat here, but try to complement in a couple of case studies. The experimental results presented here have been obtained at several different synchrotron radiation facilities, as indicated specifically for each case below.

☆ Invited article to appear in The Journal of Electron Spectroscopy and Related Phenomena Special Issue "Structure Determination and Wave-Function Analysis".

* Corresponding author.
E-mail address: fadley@physics.ucdavis.edu (C.S. Fadley).

http://dx.doi.org/10.1016/j.elspec.2014.06.004
0368-2048/

2. Some basic parameters and phenomena

2.1. Differential photoelectric cross sections for atomic orbitals in arbitrary experimental geometries

Photoelectron spectrometers, both dispersive and time-of-flight, are rapidly being developed that can simultaneously measure intensities over an increasingly broader two-dimensional angle range, as e.g. those discussed by Matsuda [2] and Matsushita [3] in this issue. One can thus ask a very basic question in studying both core- and valence- electron emission as to the precise form of the differential photoelectric cross sections involved, and how they will vary over the detection range of the spectrometer. Such variations can influence both PD and ARPES, for example. With polarized radiation for excitation, it is well known that the cross section is strongly affected by the experimental geometry, but there is no readily accessible source of differential cross sections for individual atomic orbitals such as e.g. the t_{2g} set d_{xy}, d_{yz}, and d_{zx} and the e_g set $d_{x^2-y^2}$ and d_{z^2}. A program has thus been written in our group [4] that will be made available to the community at large and which permits calculating the differential photoelectric cross sections for core and valence atomic orbitals for arbitrary experimental geometries and light polarizations. This makes use of analytical formulas developed by our group some time ago [5], to which are added a database of photoelectric cross sections and continuum-wave phase shifts. These should be generally useful to many groups in trying to estimate the relative contributions of different orbitals to in particular valence-band spectra, whether density-of-states like or momentum-resolved as in ARPES. In ARPES one certainly has additional selection rules on wave vector **k** and matrix elements that depend on the orbital makeup of a given band that are critical for describing the full dispersion curves, and these can only be assessed by more accurate photoemission calculations, for example, with the surface explicity included in a time-reversed low energy electron diffraction or so-called "one-step" picture [6]. However, atomic cross sections can nonetheless provide insight as to what bands should be strong in which directions.

As an illustrative example of these atomic orbital differential cross sections, in Fig. 1, we show some first results from this program, actually calculated for two closely-related experimental geometries we have used for soft X-ray ARPES at both the Advanced Light Source (ALS) and the Swiss Light Source (SLS). In Fig. 1(a), the experimental geometry we have used is shown, and in Fig. 1(b) the cross sections of the various d orbitals at the ca. 833 eV excitation energy used in experimental results that will be discussed in subsequent figures, for both s- and p-polarizations. Gray [1] has also considered data obtained at this photon energy. The red highlights indicate orbitals that would be directly seen strongly (solid line) or weakly (dashed line) in the precise emission direction shown in 1(a), and an "x" indicates orbitals that are not expected to be seen at all. But the fact that a given two-dimensional spectrometer might see well beyond this direction can also be judged from the forms of these profiles. The complex form of these cross section profiles makes it clear that the planning of many future experiment with variable polarization and a spectrometer accepting a wide angle range will much benefit from having these simple atomic references, and that not considering these effects could lead to erroneous interpretations. We illustrate such effects in experimental standing-wave ARPES (SWARPES) results below.

2.2. Inelastic mean free paths

In work in both solid samples looking into vacuum, or studies with a significantly high background pressure in the multi-Torr range, in what has been termed ambient-pressure X-ray photoemission (APXPS, APPS) [7,8], the inelastic mean free path (IMFP)

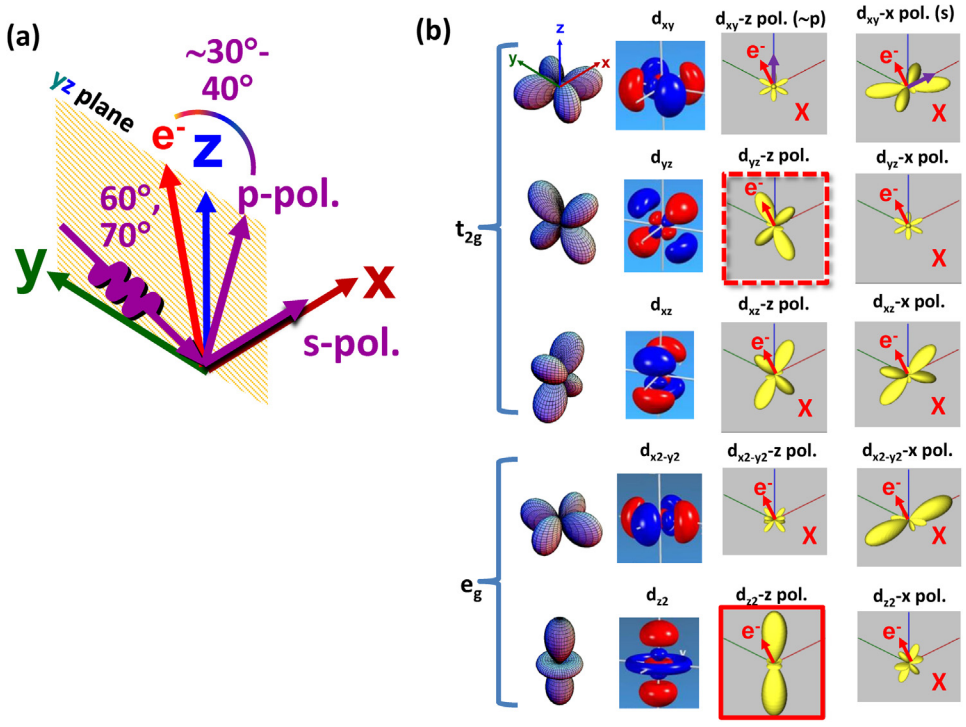

Fig. 1. Theoretical differential photoelectric cross sections for Mn 3d atomic orbitals at a photon energy of 833 eV just below the La M_5 absorption resonance. (a) The experimental geometry used in our group's soft X-ray standing-wave and ARPES measurements at the ALS and the SLS. (b) The 3d orbitals of Mn, in both angular and spatial form (plotted through contours of equal probability density), together with their three-dimensional differential cross sections in both s and p polarization, as defined in (a). Cross-section contours are all plotted on the same absolute scale: that is, the distance from the origin to the contour surface is proportional to the absolute cross section. The orbitals marked with X are not expected to contribute in, and those outlined in red/dashed red should be strongly/less strongly seen [From ref. 4].

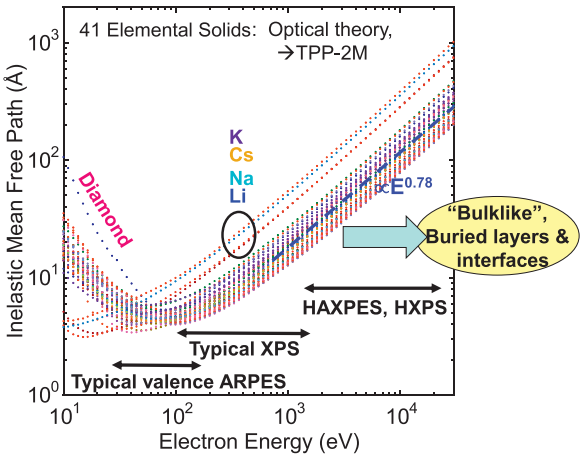

Fig. 2. Energy dependence of electron inelastic mean free paths as calculated from optical properties for 41 elements, with values closely related to the TTP-2 M formula [From ref. 9].

is of course a key parameter that can determine the effective information depth in solids, or the maximum ambient pressure that can be tolerated respectively. As one overview of the situation in solids, Fig. 2 shows some IMFPs derived from experimental optical constants for 41 elements [9]. Although there is an upturn at very low energies in the IMFPs, this does not result in IMFPs larger than 10–30 Å for most of the elements shown, and in fact is only dramatic for diamond with a very large bandgap. Direct photoemission measurements of IMFPs for both metal and metal oxide samples further confirm the conclusion that high bulk sensitivity is difficult to achieve by going to energies in the 5–10 eV regime [10,11]. Overall, these results thus make it clear that the only reliable way to study the bulk properties of materials or layers or interfaces that are buried some tens of nm below the surface is to go to higher energies in the soft X-ray (up to about 2 keV) or hard X-ray (above 2 keV) regimes. This has led to the rapid development of hard X-ray facilities at various synchrotron radiation facilities around the world [12,13].

In APPS studies [7,8], a relevant reference IMFP is that for gas-phase N_2, for which some approximate values of IMFPs as a function of energy and pressure are: 500 eV: 1 Torr, ~2 mm; 20 Torr, ~0.1 mm = 100 microns; 1 atm, ~0.003 mm = 3 microns; and 5000 eV: 1 Torr, ~12 mm; 20 Torr, ~0.6 mm = 600 microns; 1 atm, ~0.016 mm = 16 microns, where we have used the approximate energy variation of (kinetic energy)$^{0.78}$ shown in Fig. 2 for several solid elements and the expected inverse dependence on pressure for a gas. APPS is thus another aspect of photoemission that will benefit from hard X-ray excitation, by permitting the use of pressures up to 10–20 Torr or beyond, with experiments of this kind just beginning at the ALS by Axnanda et al. [14]. We will comment later on one exciting future APPS application that includes SW excitation.

2.3. Angle-resolved photoemission with soft X-ray and hard X-ray excitation

Traditional angle-resolved photoemission (ARPES) with excitation in the ca. 20–150 eV range has clearly evolved to be the technique of choice for studying the electronic structure of surfaces and complex new strongly correlated and magnetic materials. Efforts are also underway to use even lower excitation sources below 10 eV, with the aim of both increasing energy and momentum resolution and for some systems also increasing bulk, rather than surface, sensitivity. With these advances, and the development of brighter variable-polarization and femtosecond-scale light sources, together with improved spectrometers making use of time-of-flight and next-generation detectors, e.g. for spin detection, there is thus no doubt that ARPES will continue to be a leading tool of materials physics.

However, it is clear from prior experimental and theoretical work that ARPES with excitation only to 150 eV or so remains a very surface sensitive probe, thus necessitating careful *in situ* sample cleaning, cleaving, or even synthesis to avoid the measurement of surface-associated artifacts. The IMFPs shown in Fig. 2 make it clear that the only reliable way to increase bulk or buried-layer and interface sensitivity for all material types is to go to higher photon energies in the soft X-ray (ca. 0.5–2 keV) or hard X-ray (ca. 2–10 keV) regime. We will show some examples of this in both the soft- and hard- X-ray regime, with the latter operationally defined from 2 keV upward, as 2 keV is roughly the point at which Bragg-reflection crystal monochromators begin to be used instead of gratings.

For this reason, interest has grown in carrying out ARPES studies with photon energies above 500 eV [15], and going into the multi-keV range [16,17]. As one limiting factor in such higher-energy measurements, it has been known for some time that the ***k***-conserving direct-transition (DT) effects that are critical to ARPES can be smeared out by phonon effects, even though they could be observed in some systems up to 1.5 keV [18]. These effects can be estimated from a photoemission Debye–Waller factor $W(T) \approx \exp[-g_n^2 \langle u^2(T) \rangle]$, with g_n the magnitude of the reciprocal lattice vector involved in a given DT and $u^2(T)$ the one-dimensional mean-squared vibrational displacement at temperature T. Several more recent studies have explored the systematics of such measurements as a function of photon energy, temperature, and polarization for some simple test materials [15,16,19–21], and with more accurate first-principles one-step modeling [22]. It is only fairly recently that it has been pointed out by Gray et al. that ARPES can be carried out in the multi-keV hard X-ray range (HARPES), and in fact going up to 6 keV for W as a test case [16]. Some other limitations of both soft X-ray ARPES (SARPES) and HARPES are discussed in more detail elsewhere [17,23]. These include making allowance for the photon momentum in ***k***-conservation and recoil effects that can shift features and smear them in energy, with the simplest estimate of the recoil energy for an assumed single-atom of mass M being $E_{\mathrm{recoil}} \approx \hbar^2 k^2/2M \approx 5.5 \times 10^{-4} (E_{\mathrm{kin}}\,(\mathrm{eV})/M(\mathrm{amu}))$, where k is the magnitude of the photoelectron wave vector. Advantages of SARPES and HARPES beyond the deeper probing depth include less ***k*** broadening perpendicular to the surface due to inelastic scattering and the ability to describe the final state as a free electron. Two of the key parameters involved in assessing ARPES at higher energies are summarized in Fig. 3, where (a) shows isocontours of $W(T) = 0.5$, corresponding to ~50% ARPES-like direct transitions, as a function of Debye temperature, atomic mass, and electron kinetic energy, and (b) shows recoil energy shifts as a function of atomic mass and kinetic energy. The recoil shifts are probably conservative for many cases, as there will always be some "recoil free" excitation, whose fraction can in fact be estimated from the $W(T)$ value, as in Mossbauer spectroscopy. This figure can be used as an approximate gauge of how high in energy ARPES can be carried out, but examples exist where $W(T)$ represents a too-conservative estimate [16,17], and more accurate modeling that is now becoming possible will be needed to be fully quantitative concerning this [22]; we illustrate what this modeling can do below.

As an example of the utility of the free-electron final-state model, Fig. 4 shows a broad 29° scan of HARPES from W(1 1 0) at a photon energy of 2500 eV and a temperature of 90 K, for which $W(T) \approx 0.65$. Several Brillouin zones are spanned in this data and the overlying theory curves were obtained by simply making direct transitions from the W band structure to a free-electron

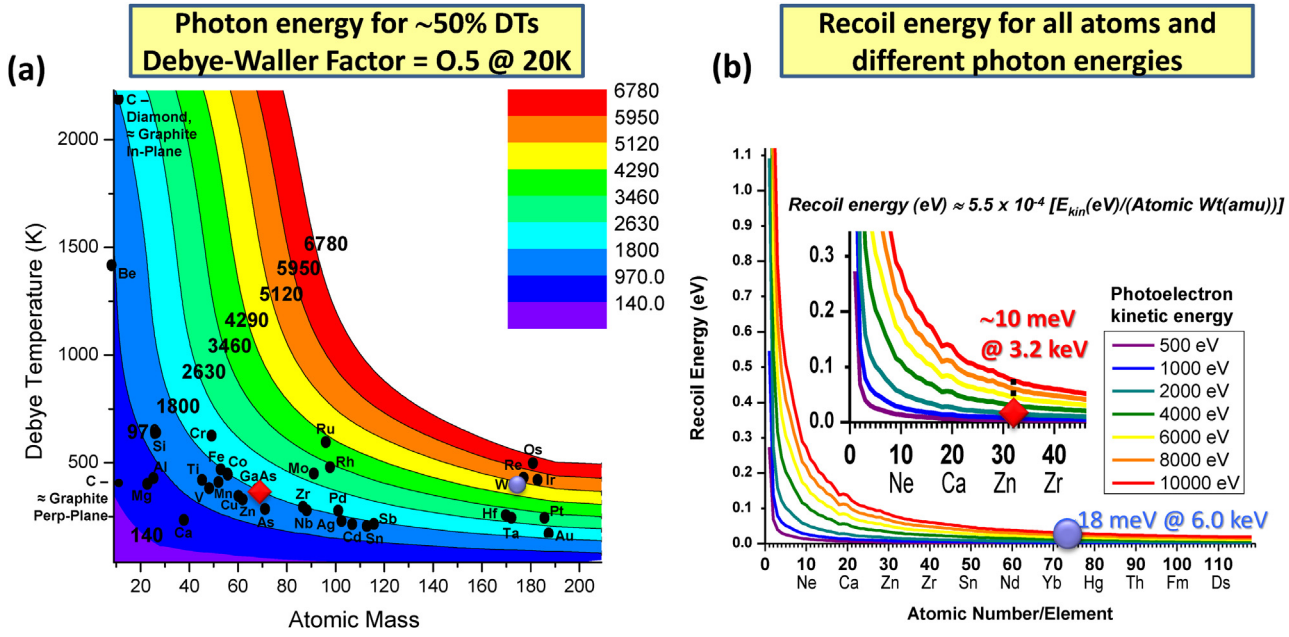

Fig. 3. Calculated parameters for estimating the feasibility of ARPES at higher energies, including (a) contours for various photon energies to yield a photoemission Debye–Waller factor $W(T)$ of 0.5 at 20 K, and (b) the recoil energy for all atoms as a function of photon energy. Values for two first demonstration cases W and GaAs studied with hard X-rays [16] are highlighted [From refs. 17 and 21].

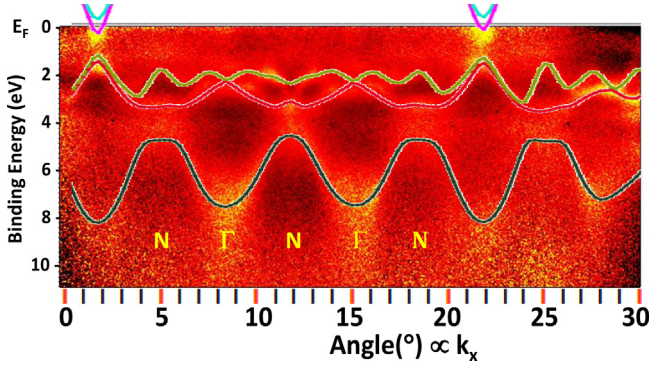

Fig. 4. Extended-angle-range hard X-ray angle-resolved photoemission (HARPES) from W(1 1 0) at a photon energy of 2500 eV and temperature ≈90 K: the experiment represents multiple detector images tiled together; the overlying curves are based on **k**-conserving transitions between the W band structure and free-electron final states. The surface normal is near to the mirror symmetry line in the pattern at ca. 12 degrees, and some approximate repeated Brillouin zone positions scanned near this symmetry line are also indicated. Experimental data from the ALS, beamline 9.3.1 [From ref. 24].

final state [24]. The curvature of the arc of the final wave vector in k-space accounts for the fact that the bands probed do not repeat, as different Brillouin zone regions are sampled in different parts of this plot. The mirror symmetry about 12° is due to the fact that this is near the sample normal, and in fact the high-symmetry directions sampled over ~5° to ~19° are approximately N-Γ-N-Γ-N, as indicated on the figure. Such effects are explained in more detail for a different experiment on W elsewhere, including a drawing in k-space [16]. For convenience in converting angle scales to wave vector in subsequent figures at various photon energies, $k(\text{Å}^{-1}) = 0.512(E_{\text{kin}}(\text{eV}))^{1/2} \approx 0.512(h\nu(\text{eV})^{1/2})$ for valence-level emission.

As an indication of a recent advance in quantitatively modeling phonon effects in higher-energy ARPES [22], Fig. 5 shows experimental results from W(1 1 0) for an 870 eV photon energy at four different temperatures for (a)–(d) experiment, (e)–(h) less accurate modeling from a prior study using complex scattering phase shifts [21], and (i)–(l) more accurate theoretical modeling via the coherent potential approximation (CPA) [25]. It is clear that the CPA modeling correctly predicts the buildup of the density-of-states-like (DOS-like) features that are characteristic of typical XPS spectra as temperature is raised. Panel (a) also confirms the semi-quantitative validity of using a free-electron final-state model to predict the ARPES curves, but it is important to keep in mind that it provides no information on relative intensities, which must be derived from something like the one-step theory shown in this figure, or at a more approximate level from differential photoelectric cross sections such as those shown in Fig. 1.

2.4. X-ray optical effects, including standing waves, resonant excitation, and total reflection

An additional set of new experimental directions in photoemission involves making use of various X-ray optical effects that can selectively tune the electric field profile in the sample and/or its element specificity. Our group has written a versatile program for calculating such effects [26].

As noted previously, Gray [1] has presented an excellent overview of recent developments that make use of a standing wave (SW) created above samples synthesized as, or on top of, multilayer mirrors. A typical sample configuration is shown in Fig. 6, with the sample as a multilayer mirror whose repeat bilayer spacing is d_{ML}, yielding finally for the first-order Bragg reflection a standing wave period $\lambda_{\text{SW}} = d_{\text{ML}}$. The SW can be scanned through the sample in one of three ways, as indicated in Fig. 6: scanning angle over the Bragg reflection through a rocking curve (RC) [27], scanning photon energy through the Bragg reflection [28], or tuning to the Bragg reflection and scanning the X-ray spot over a wedge profile sample grown on top of the mirror [29]. The first two scan the wave over half of its period, and the wedge scan can involve multiple periods.

As an additional aspect of such SW studies, tuning the photon energy to somewhere near a resonance can enhance reflectivity significantly, as done by Gray et al. in a study of the $SrTiO_3/La_{0.7}Sr_{0.3}MnO_3$ interface in a multilayer sample [27]; here,

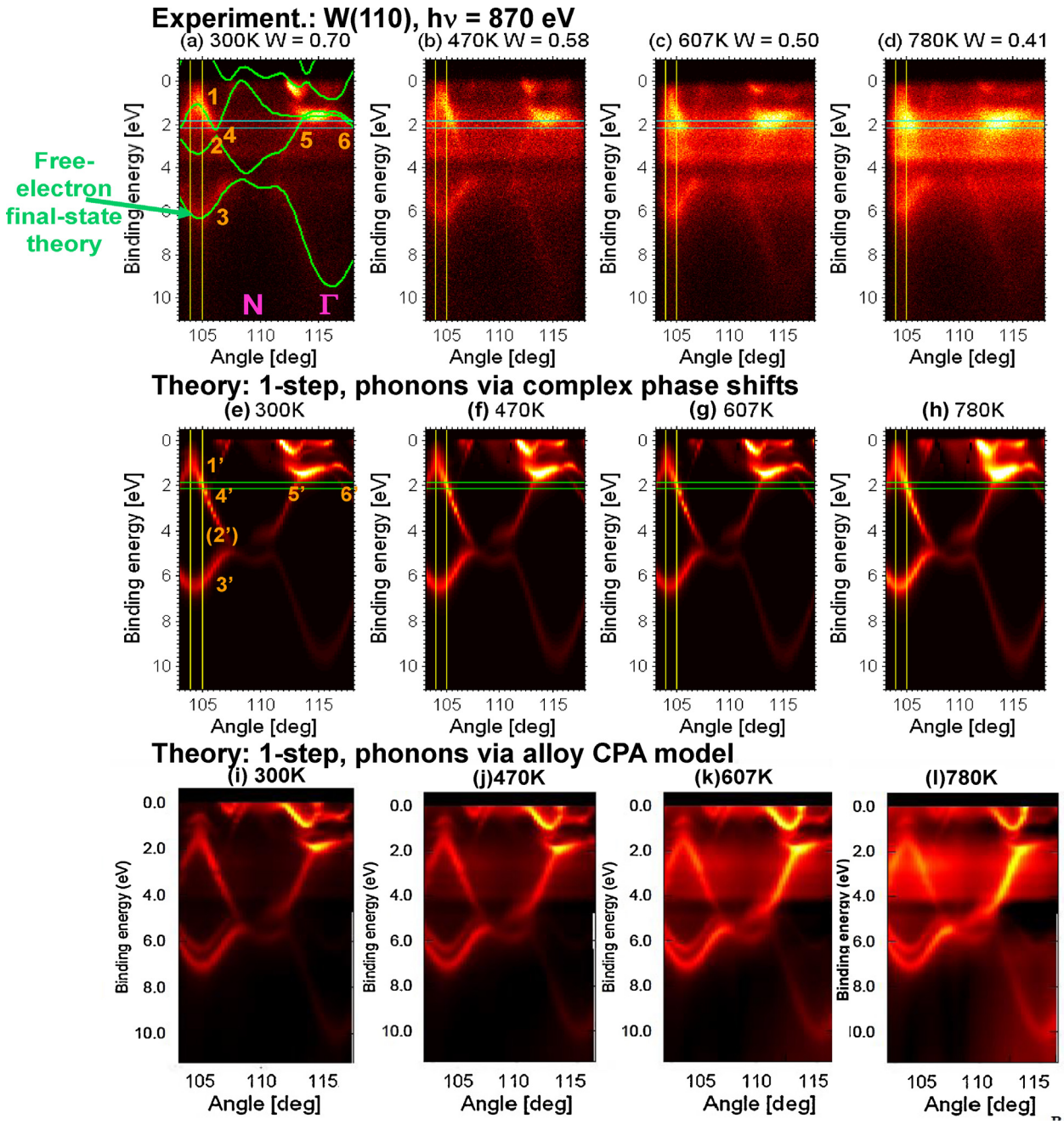

Fig. 5. Effects of temperature on ARPES with soft X-ray excitation for W(1 1 0) over 300 K to 780 K with 870 eV excitation: (a)–(d) the experimental data at four temperatures, with Debye–Waller factors $W(T)$ indicated, and free-electron final-state modeling as green curves. (e)–(h) One-step photoemission calculations with phonon effects modeled through complex phase shifts. (i)–(l) One-step photoemission calculations with improved phonon modeling via the coherent potential method. Experimental data from the ALS, Beamline 4.0.2. The weak pairs of horizontal and vertical green lines have been used elsewhere as integration limits to generate special spectral regions for more detailed analysis [From Refs. [21] and [22]].

the energy was tuned to just below the La M_5 resonance. As a second aspect of the possibilities from such tuning, Fig. 7(a) shows a plot of the index of refraction of Gd over its analogous M_5 resonance, and Figs. 7(b and c) the variation of the calculated electric field strength $|E^2|$ as a function of depth and incidence angle for a similar $SrTiO_3/GdTiO_3$ multilayer [30]. From the position just below the resonance at 1182 eV (Fig. 7(b)) to one about the same distance above at 1187 eV (Fig. 7(c)), the position of the SW maximum at the Bragg reflection moves from a position near the top of the $SrTiO_3$ layer to a position near the $SrTiO_3/GdTiO_3$ interface. This thus illustrates a second aspect of tuning SW properties by varying photon energy.

As a third useful method for doing photoemission with enhanced depth resolution, going into the total reflection regime has for some time been utilized to enhance surface sensitivity and reduce inelastic backgrounds in XPS [31]. But additional interference effects can provide useful structural information on going into total reflection, with this possessing the advantage that it can be applied to any material, but in particular, bilayer or trilayer samples that are simpler to grow than multilayers. We illustrate this in Fig. 8 with some experimental data and theoretical calculations for a bilayer sample of a Mn-doped ferroelectric $Bi(Fe_{0.95},Mn_{0.05})O_3$ on top of a Ce-doped Mott insulator $(Ca_{0.96}, Ce_{0.04})MnO_3$ [32], a system recently studied as leading to strong ferroelectric control

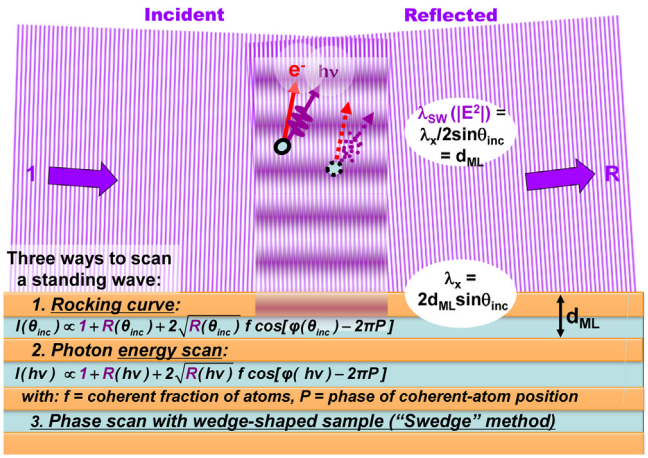

Fig. 6. Schematic illustration of the formation of a standing wave in first-order Bragg reflection from a multilayer mirror, together with the equations describing the standing wave period λ_{SW}. The standing wave can be scanned through the sample, which might be the mirror, or grown on top of the mirror, in the three ways indicated: a rocking curve, a photon energy scan, or a wedge scan. See further discussion of these methods in Gray, ref. 1.

of the Mott insulator–metal transition [33]. In Fig. 8(a), the sample configuration is shown, with the photon energy taken to be 2.8 keV, in Fig. 8(b) the expected electric field variation with depth and incidence angle, in Fig. 8(c) the measured and calculated photoemission intensity profiles for Bi 4f and Ca 2p, representing the two active sample layers, and finally in Fig. 8(d) the comparison of these two intensities in an enlargement from Fig. 8(c). The oscillations are due to reflections and interference at the surface and the two buried interfaces in the sample, and the peaks in intensity near 0.9° to the concentration of electric field near the surface, an effect first observed and explained in photoemission by Henke [34]. Important additional features are the differences in phase of the oscillations for Bi and Ca shown in Fig. 8(d), which should be useful in deriving depth-dependent interface information for this and other similar samples in future studies. In fact, similar effects are seen in hard X-ray reflection and emission and have been used to study few-layer systems [35], but with less depth sensitivity due to the longer penetration depths of X-rays compared to electrons, and less chemical sensitivity via that which is seen in photoemission through chemical shifts in core levels.

We now turn to a few more specific examples of applications of these phenomena and techniques.

3. Hard X-ray angle-resolved photoemission: application to a magnetic semiconductor

We will now briefly discuss a first application of HARPES to the elucidation of the electronic structure of a material over which some controversy has existed: the prototypical dilute magnetic semiconductor (DMS) $Ga_{1-x}Mn_xAs$, with $x \approx 0.03$–0.06. The key question here is the nature of the Mn-induced states, and whether they represent a narrow impurity band that is separated cleanly from the GaAs p valence bands, or whether these states are merged

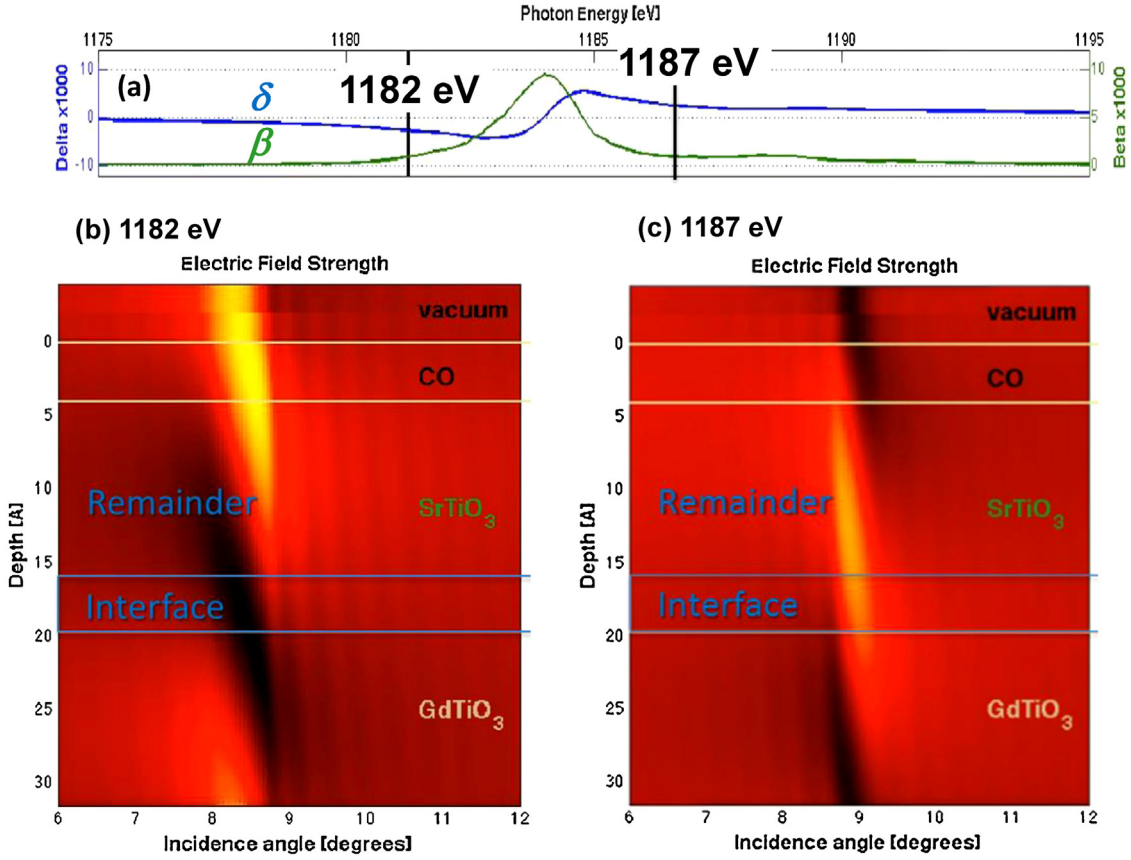

Fig. 7. X-ray optical calculations using the program of ref. 26 of the effect of tuning photon energy to a position below and above the Gd M_5 absorption resonance on the location of the standing wave, for a 20-bilayer multilayer of $SrTiO_3$ and $GdTiO_3$ with bilayer thickness of 35.5 Å. (a) The variation of the real (δ) and imaginary (β) parts of the index of refraction over the Gd M_5 absorption resonance, from experimental X-ray absorption data and Kramers–Kronig analysis. (b) and (c) The depth distribution of the standing-wave electric field intensity as the incidence angle is scanned through the 1st-order Bragg reflection of the multilayer, for the two photon energies 1182 eV and 1187 eV. The first $SrTiO_3$ layer has been divided into an "interface" region and a "remainder" for additional theoretical analysis. See also Fig. 11 [From ref. 30].

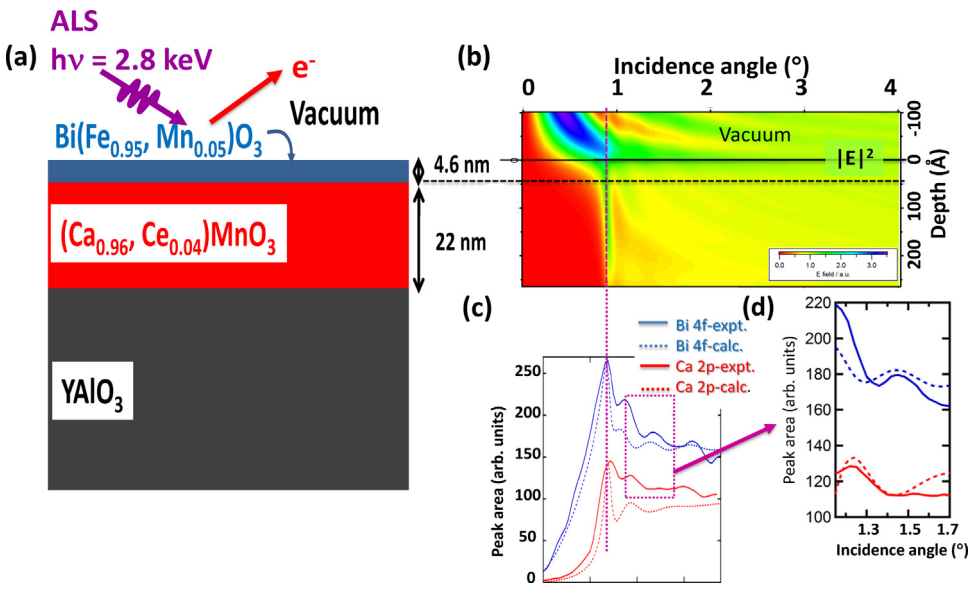

Fig. 8. The effect of scanning the incidence angle of 2.8 keV photons into total reflection on the Bi 4f and Ca 2p photoelectron intensities from a bilayer of Mn-doped $BiFeO_3$ and Ce-doped $CaMnO_3$. (a) The sample configuration. (b) The calculated depth dependence of the electric-field intensity. (c) With the same angle scale as (b), the variation of the Bi 4f and Ca 2p photoelectron intensities, experimental and simulated with our program [26] for the ideal sample geometry, without optimization of structural parameters. (d) A blowup from (c), with curves shifted vertically to more closely compare experiment and theory, illustrating also the phase differences in the interference fringes between the $BiFeO_3$ and $CaMnO_3$ layers. Experimental data from ALS Beamline 9.3.1 [From ref. 32].

with the GaAs impurity bands. In the former case, the so-called double-exchange mechanism would be active in producing ferromagnetism and in the latter, it would be what has been referred to as p-d exchange. Gray et al. [36] have studied a sample with composition $Ga_{0.97}Mn_{0.03}As$, with 3.2 keV photon energy; beyond a light acid etch in air to remove surface oxide, no other surface preparation was done, illustrating a key advantage of more bulk sensitive HARPES. In Fig. 9, the HARPES data from GaAs and $Ga_{1-x}Mn_xAs$ are compared, with very accurate one-step photoemission calculations shown in (a) and (b), experimental results in (c) and (d), and the angle-resolved intensity from a core-like, predominantly As 4s, band at about 12 eV that exhibits hard X-ray photoelectron diffraction (HXPD) effects in (e) and (f), respectively. The intensity distributions of the $Ga_{1-x}Mn_xAs$ are in all panels smeared out relative to those in GaAs, as might be expected from the presence of the Mn atoms which disturb the long-range periodicity. One-step theory is in agreement with experiment in predicting these differences, with other theoretical results and analysis being presented elsewhere [36]. Further analysis of the ***k***-resolved results, including angle-averaged differences between GaAs and $Ga_{1-x}Mn_xAs$, and special attention to the region very near E_F [36] permit concluding that we must for this material consider both p-d exchange

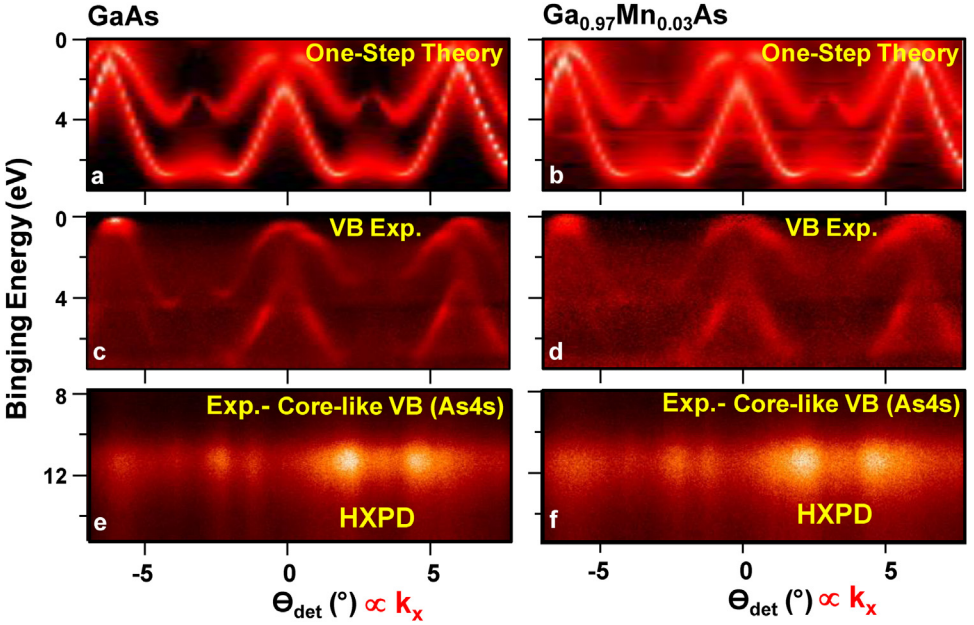

Fig. 9. Hard X-ray angle-resolved photoemission (HARPES) at 3.2 keV photon energy from GaAs and the magnetic semiconductor $Ga_{0.97}Mn_{0.03}As$, with data obtained at SPring-8. (a) and (b) Accurate one-step photoemission theory for the two materials. (c) and (d) The analogous experimental results. (e) and (f) Experimental results for the deeper band at about 12 eV, which is very core-like and shows HXPD effects which are displaced from the high-symmetry directions in the ARPES due to the photon momentum effect on the latter [From ref. 36].

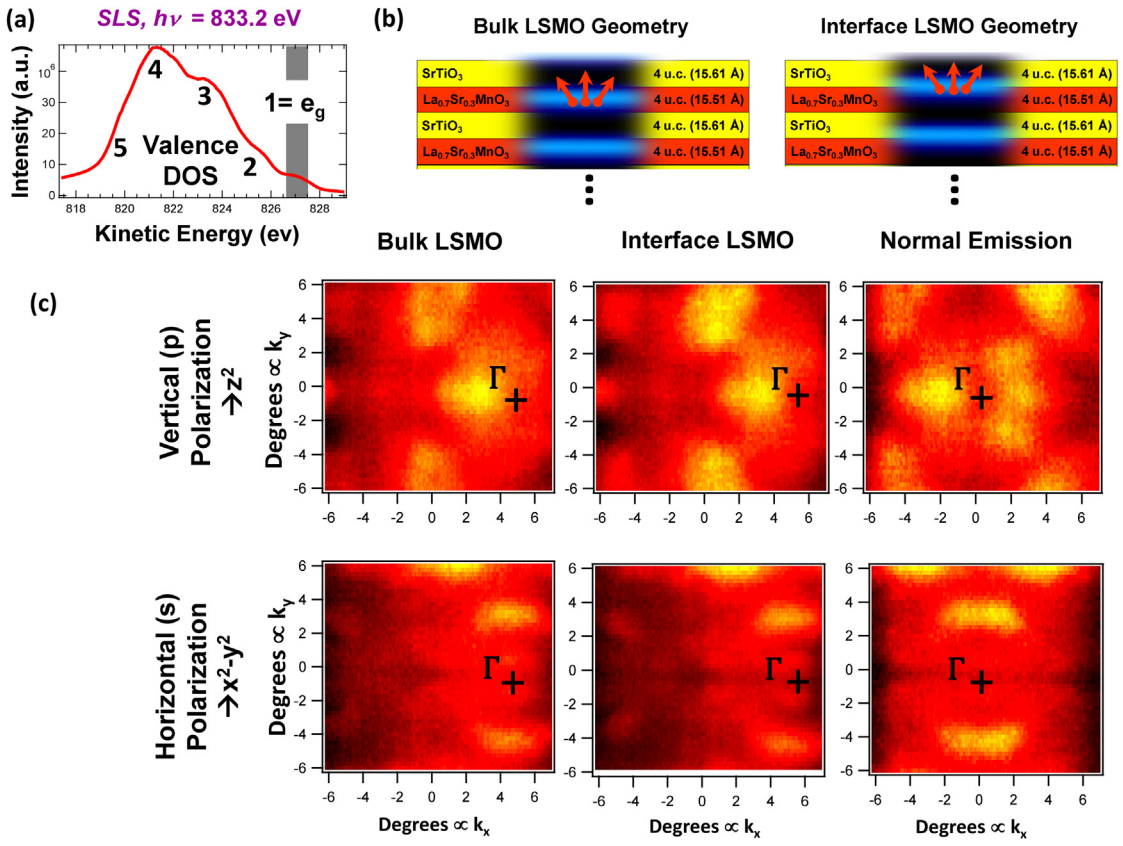

Fig. 10. Variable-polarization standing-wave ARPES (SWARPES) results from the $SrTiO_3/La_{0.7}Sr_{0.3}MnO_3$ (STO/LSMO) multilayer discussed in detail by Gray in ref. 1, obtained in the experimental geometry of Fig. 1. A density-of-states plot for reference, with five features labelled, included 1 which represents Mn 3d e_g-derived states. (b) The two standing-wave geometries selected by varying incidence angle, one emphasizing the interior of the LSMO layer and the other the STO/LSMO interface. (c) The k_x-k_y SWARPES patterns for s- and p- polarizations, with the dominant Mn 3d component expected, based on the differential cross sections in Fig. 1. Experimental data are from SLS, ADDRESS Beamline [From ref. 42].

and double exchange to explain its ferromagnetism. This study thus represents a first application of HARPES to a complex system whose electronic structure was in debate, and it suggests other such opportunities in the future. The future prospects and limitations for HARPES have been discussed in more detail elsewhere [17,23].

Having mentioned HXPD for the As 4s band in Fig. 8(e–f), we also should note that such effects have been considered theoretically by Winkelmann et al. [37], including an article in this issue [38]. Briefly, the features in HXPD patterns resemble more strongly Kikuchi bands, and it appears that a dynamical Bragg scattering approach has advantages for theoretical modeling compared to the more traditional cluster approach, as e.g. used in the online EDAC program [39]. Beyond this, HXPD is suggested to have some distinct advantages in providing element-specific local structure, especially for dopants in materials such as $Ga_{1-x}Mn_xAs$, to which it has in fact recently been applied [40].

4. Soft X-ray ARPES with resonant and standing wave excitation: application to complex oxide multilayers

Standing-wave ARPES (SWARPES) has been discussed in detail by Gray [1], in particular for the system $SrTiO_3/La_{0.7}Sr_{0.3}MnO_3$ [41] but as an illustration of which also exhibit the qualitative form of the differential cross section as discussed in connection with Fig. 1, Fig. 10 shows some s- and p- polarization SWARPES results for a $SrTiO_3/La_{0.7}Sr_{0.3}MnO_3$ multilayer over a window of about $6^\circ \times 6^\circ$, and for X-ray incidence angles corresponding to two different positions of the standing wave relative to the $SrTiO_3/La_{0.7}Sr_{0.3}MnO_3$ interface, as well as for normal emission well away from Bragg reflection [42]. In Fig. 10(a) is a reference spectrum indicating several bands of energy that are associated with valence states of different character, and which are discussed in detail by Gray et al. [1,41]. Here, we will focus on the band of energy with strong Mn 3d e_g character closest to the Fermi level. In Fig. 10(b), the two positions of the SW, are qualitatively indicated, and in Fig. 10(c) the ARPES results for this band, as resolved in k_x–k_y, are shown. Note the reduced intensity in the nodal plane for s polarization, as expected from the cross sections of Fig. 1, as well as the lack of left-right symmetry for p polarization and normal emission due to the canting of the emission direction relative to the polarization (cf. Fig. 1(a)). Such effects, including asymmetries in the data, will arise in many current experimental ARPES geometries, again reinforcing the conclusion that an accurate allowance for these fundamental cross section effects, or more accurate calculations of them including photoelectron diffraction and/or **k** conservation plus matrix elements is important for future studies.

As a further illustration of X-ray optical effects, we show some preliminary soft X-ray data for a $SrTiO_3/GdTiO_3$ (STO/GTO) multilayer in Fig. 11 [30]. The STO/GTO interface is known from work by Stemmer et al. [43] to exhibit a two-dimensional electron gas (2DEG) for certain thicknesses of GTO sandwiched between STO. So a key question is whether the 2DEG can clearly be seen in soft X-ray ARPES using SW excitation. Fig. 11(a) shows the multilayer sample we have studied, carrying out rocking curve measurements to vary the SW position. Fig. 11(b) indicates the electronic structure of bulk GTO, which, via the canted octahedra in its crystal structure exhibits an upper and lower Hubbard band (UHB and LHB), with the lower filled and expected to be seen in photoemission. Fig. 11(c) shows ARPES data at a Ti 2p-3d resonant energy of ~465 eV, and we see two features near E_F, one at about 0.7 eV binding energy that

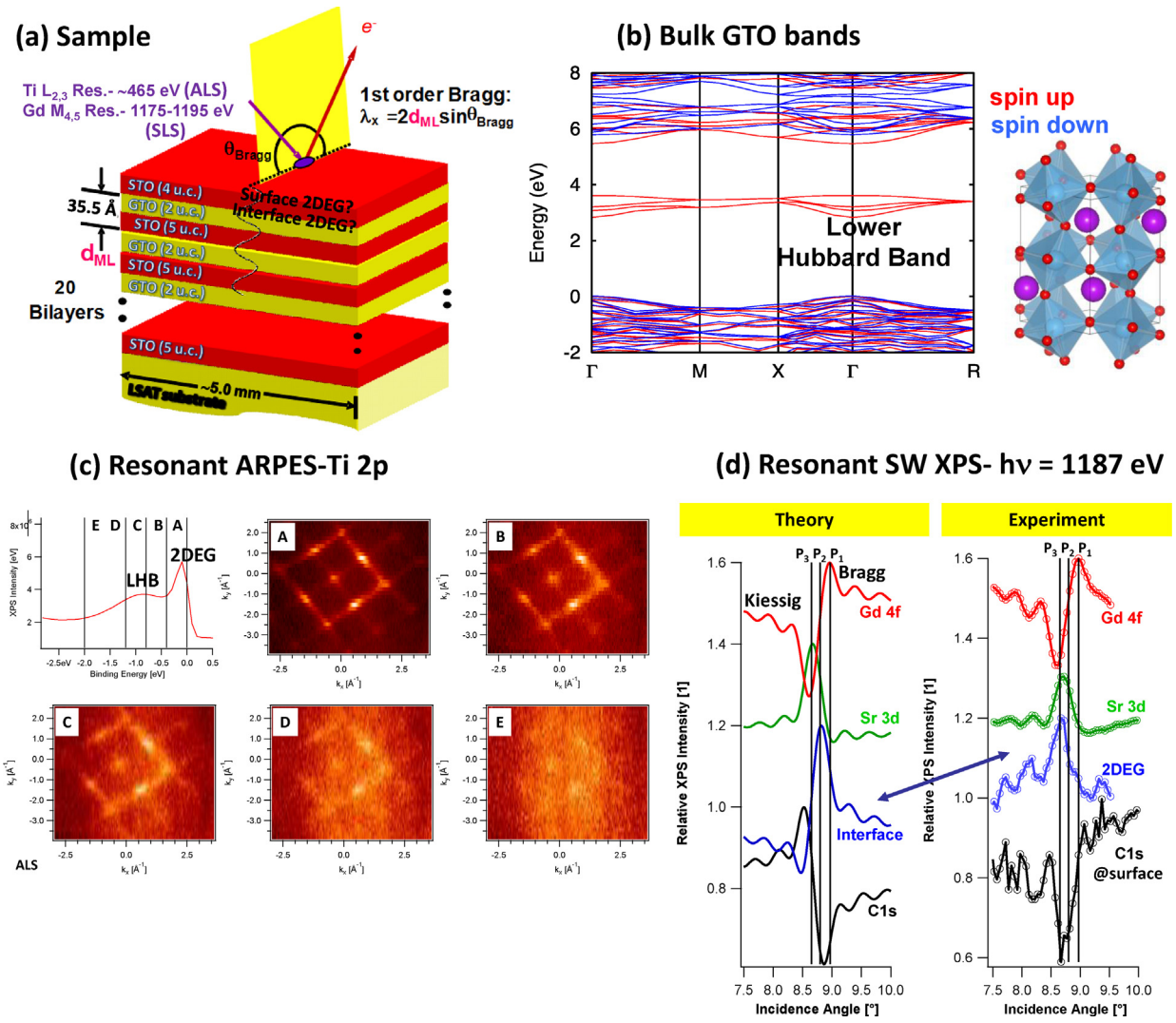

Fig. 11. Experimental results from a combined standing-wave and resonant photoemission study of a $SrTiO_3/GdTiO_3$ (STO/GTO) multilayer. (a) The sample configuration, with the Ti and Gd resonance energies used indicated. (b) The electronic structure of bulk $GdTiO_3$, including a section of the crystal structure indicating the tilted TiO_6 octahedra that lead to the filled lower Hubbard band (LHB) shown. (c) Ti 2p-resonant ARPES over two features near the Fermi level, as binned in five separate regions A to E. (d) Gd 3d-resonant standing-wave photoemission at 1187 eV (cf. Fig. 7(c)), including rocking curves for the Gd 4f, Sr 3d, and C 1s (surface impurity) core levels, and valence-level intensity over region A, derived by peak fitting. From this the LHB and 2DEG (region A) in STO near the STO/GTO interface are clearly identified. Experimental data are from the ALS, Beamline 7.0.1 and SLS, ADDRESS [From ref. 30].

can readily be identified as the LHB, and one at about 0.2 eV and extending to E_F that we tentatively identify as the 2DEG. These features are only seen clearly on resonance and so both clearly have a strong Ti 3d makeup; they also have very similar dispersion curves, suggesting strong admixing in character that is confirmed by LDA calculations by Van de Walle et al. [30]. But is the 2DEG really at the interface, or can it be at the surface of the sample, arising in the final STO layer, as has been observed in low-energy VUV ARPES [44]? This is easily resolved by measuring rocking curves with an incidence energy of 1187 eV just above the Gd M5 edge that X-ray optical calculations tell us should result in a SW position centered on the interface, via the technique that has been introduced in Fig. 7. Fig. 11(d) shows these rocking curve results, and by comparing theoretical and experimental core-level curves from elements in different layers with the curves from what we assign to the 2DEG state, we can very clearly see that this state is at the buried STO/GTO interface. Note in particular that the 2DEG rocking curve is very different from that of C 1s (a surface impurity on top of the last STO layer) and from that of Gd 4f that arises over the bulk of the GTO layer. Thus, we can conclude that the 2DEG is localized at the buried interface and not at the surface, as seen previously with VUV ARPES [44], and is also primarily located in the STO. These results thus constitute an illustrative example of what can be done for other systems by mixing different resonant effects: standard resonant photoemission to enhance a given atom's contributions to ARPES, tuning to a resonant energy to maximize reflectivity and thus SW effects, and tuning above or below a given resonance to move the position of the SW more dramatically.

5. Standing-wave photoemission: application to the study of solid-gas and solid-liquid interface reactions at ambient pressures

Our group has also recently begun to pursue the possibility of using SW ambient pressure photoemission (SWAPPS) to directly study the sub-nm interface region near a solid/gas or solid/liquid interface [45]. This region is critical to any surface reaction, catalytic reaction, or electrochemical process, and so is of high importance in many areas of environmental and energy research. For example, the electrochemical double-layer has been studied for over 100 years, and is not yet understood [46,47].

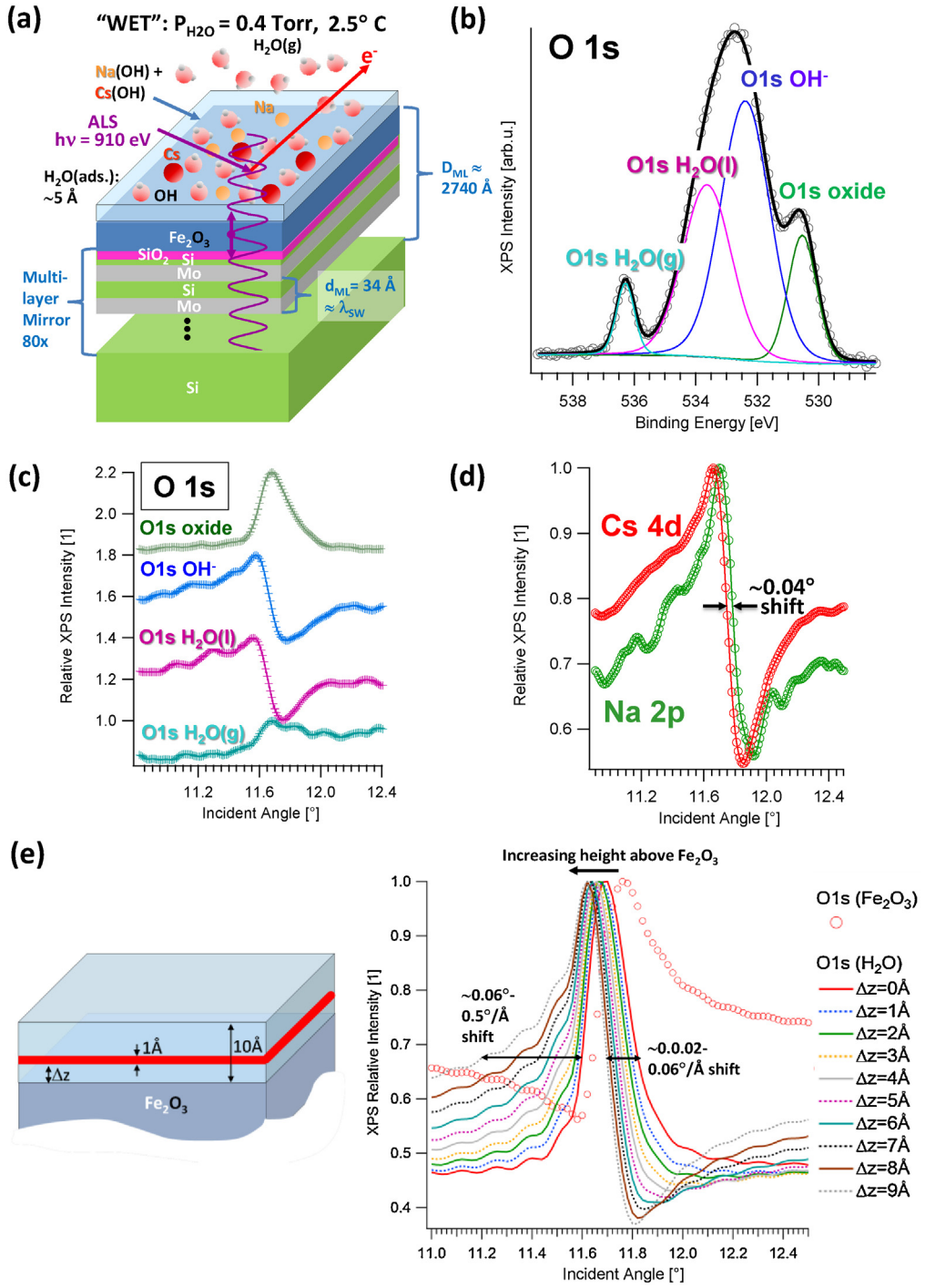

Fig. 12. First experimental results for standing-wave ambient pressure photoemission (SWAPPS) from an Fe_2O_3 film grown on a Si/Mo multilayer mirror whose surface was exposed to CsOH, NaOH, and water vapor at 400 mTorr and 2.5 °C. The SW is moved through the surface by scanning the incidence angle through the 1st order Bragg condition (cf. Fig. 6). (a) The sample configuration. (b) A typical O 1s spectrum, with four distinct chemical species unambiguously identified. (c) The variation of the O 1s intensities of the four species, with all showing strong and distinct variations as the standing wave moves by half of a cycle through the interface. (d) A comparison of the rocking curves of Cs and Na, indicating a shift of ~0.04° near the Bragg angle and different behavior in the wings of the curves. (e) Theoretical calculations of rocking curves for a $\Delta z = 1$ Å-thick delta layer as a function of its position from the Fe_2O_3 surface, compared to that expected from O 1s in Fe_2O_3 as a fixed reference. Experimental data are from ALS, Beamline 11.0.2 [From ref. 45].

We have very recently obtained the first SWAPPS data for water reacting with NaOH and CsOH on the surface of a thin film of Fe_2O_3 grown on a Si/Mo multilayer mirror, at a pressure and temperature for which the surface can be considered to be "wet", with a thin film of "liquid-like" water about 10 Å in thickness on the surface [45]. Fig. 12(a) shows the sample configuration, and 12(b) a typical O 1s spectrum with four distinct chemical components clearly resolvable, including water in the gas phase above the sample. For the pressure of 400 mTorr and temperature of 2.5 °C we have used, the adsorbed water layer is found to be about 8 Å thick by analyzing relative core peak intensities using the SESSA program [48]. In Fig. 12(c), it is remarkable that all four components show the effects of the SW scanning through the surface, including even the gas-phase water, and that they each have distinct shapes. Fig. 12(d)

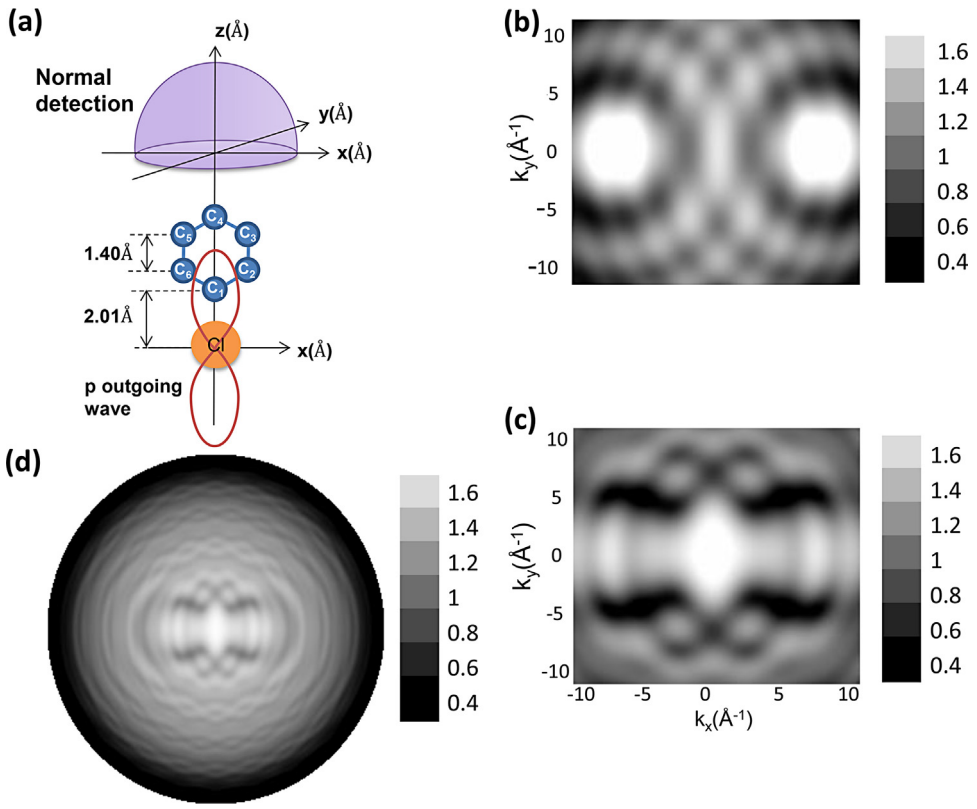

Fig. 13. (a) The normal emission experimental geometry for simulating photoelectron holography in Cl 1s emission from chlorobenzene. (b) The calculated photoelectron diffraction pattern = hologram using a three-atom cluster of Cl emitter and C_2 and C_6 scatterers, as in ref. 65, which is in excellent agreement with these prior calculations. Note the two dominant forward scattering peaks, with their overlapping 1st, 2nd, 3rd, 4th and 5th order diffraction rings. (c) As (b), but for the full seven-atom cluster, and with significant differences seen, including the much less visible forward scattering peaks seen in (b). (d) As (c) but over a full hemisphere of detection, corresponding to a radius of 21.11 Å-1 in the k_x-k_y plane. The color bar indicates the relative amplitudes of the relative amplitudes of the hologram $H\left(\vec{k}\right)$. [From ref. 49].

now compares the rocking curves for Cs 4d and Na 2p intensities, and we find a small but reliable shift of 0.4° in the steeply sloping regions of the two curves near the Bragg angle of the multilayer, but also a different shape in the wings away from these regions, with Cs having higher intensity both below and above the Bragg angle. To provide some insight into the depth resolution of these measurements, Fig. 12(e) presents some model calculations of the shapes of rocking curves for a "delta layer" of 1 Å thickness that could be represent either Cs or Na emission, as a function of distance above the Fe_2O_3 surface. These indicate that a 0.4° shift at the maximum slope region can be associated with a 2 Å difference in position, but more so that the behavior in the wings of the rocking curve are also very sensitive to vertical position, showing even larger changes in angular width on the low-angle side of the rocking curve. Thus, we can tentatively conclude that Cs is on average about 2 Å farther from the Fe_2O_3 surface, and probably also has a broader distribution in z, although a more detailed analysis incorporating some assumed distributions in depth (e.g. rectangular or Gaussian) for both Cs and Na will be necessary to be fully quantitative, and this is in progress [45].

These results thus point to the use of such SWAPPS measurements for studying the interface region of surface reactions in a much more precise and both element- and chemical state- resolved way than has previously been possible, with a broad range of applications including catalysis, as well as energy and environmental research.

6. Photoelectron holography: making molecular movies with free-electron laser excitation

As a final future perspective related to structure, photoelectron holography is discussed in the article by Matsushita in this issue, and we will here only briefly point out one future possibility for it, with some theoretical simulations to assess feasibility and optimal experimental parameters [49]. Photoelectron holography (PH) was originally developed in the surface science community for studying near-surface atomic structure. It was first suggested by Szöke [50] and more concretely realized by Barton [51] that a core-level photoelectron diffraction (PD) pattern could be considered to be a hologram which could in turn be mathematically inverted to produce an image of the atoms around the emitter. Barton [52] extended this idea into a more powerful multi-energy formulation that reduces image distortions and artifacts, including twin images. There have by now been a number of papers discussing the unique merits and limitations of PH compared to other atomic structure methods, including various refinements in the imaging algorithms to further improve structural accuracy [53–61]. Somewhat later, it was also realized that PD effects are present in the angular distributions in core-level photoemission from free molecules [62,63] and that the multiple-scattering theoretical methodologies developed for studies of surface species could be used with small modifications to describe such data [63,64].

Most recently, with the development of several free-electron laser facilities in the world with unprecedented brightness and pulse widths in the femtosecond regime, it has been pointed out by Krasniqi et al. [65] that PH has the potential for producing real-time "movies" of atomic motion in molecular dissociations and reactions, e.g. as initiated by some sort of pump pulse. These authors have also presented theoretical calculations of single-energy PD patterns and atomic holographic images for a test-case molecule (chlorobenzene) as excited by a hard X-ray so as to produce photoelectrons at ~1700 eV in a feasible experimental geometry and with two different radiation polarizations. In a recent paper from

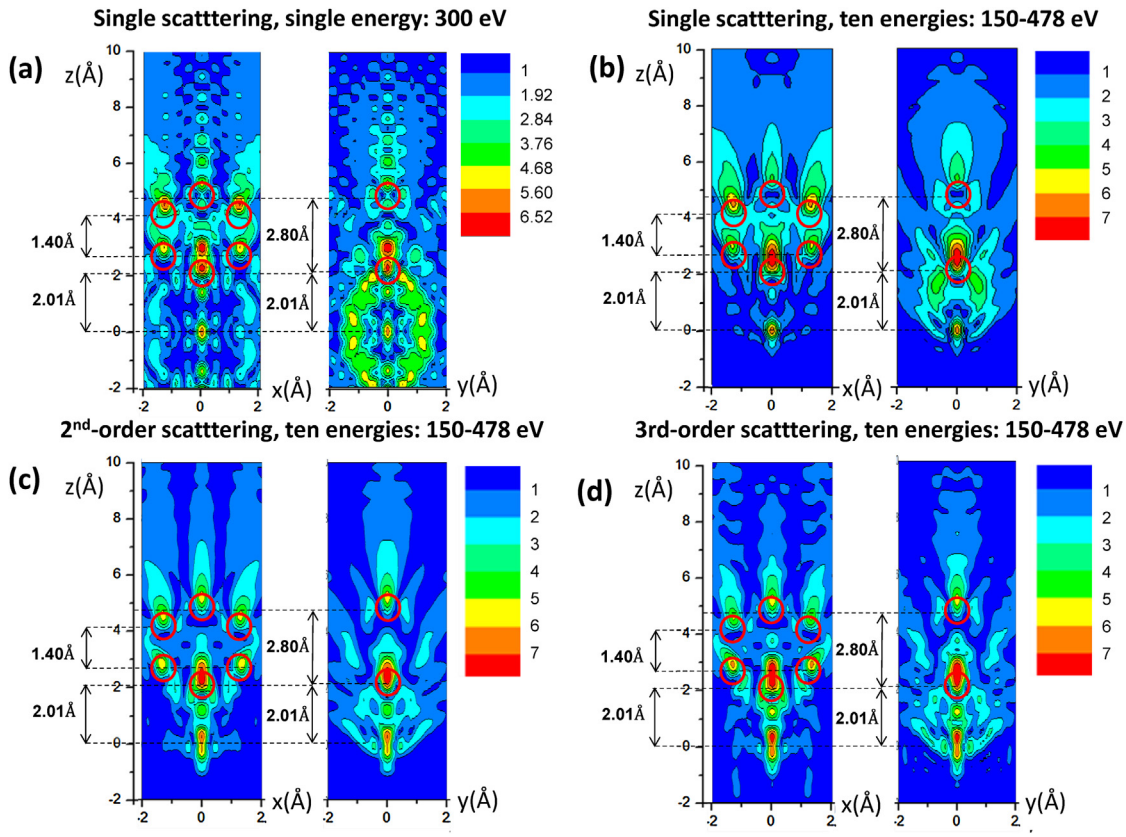

Fig. 14. Holographic images through the two high-symmetry planes *x-z* and *y-z* of the chlorobenzene molecule based on photoelectrons of low kinetic energy centered on about 300 eV and different orders of scattering: (a) single energy of 300 eV, 1st order scattering only, (b) ten energies over 150–478 eV, 1st order scattering only; (c) ten energies over 150–478 eV, up to 2nd-order scattering; (d) ten energies over 150–478 eV, up to 3rd-order scattering [From ref. 49].

our group, the prior work by Krasniqi et al. has been extended so as to explore improving the quality of the reconstructed image of the molecular structure in two ways: by exploring the choice of outgoing photoelectron kinetic energy and by asking whether single or multiple photoelectron kinetic energies should be employed to optimize the image quality [49]. It is important to note however, that going to lower-energy photoelectrons to reduce the degree of forward scattering and enhance the degree of back scattering, and using multiple energies to reduce twin images and reduce image artifacts, have both been found to be more beneficial in several prior PH studies of solids and surfaces [52,53,58–60].

As in the prior study [65], the emitter was the chlorine atom in the chlorobenzene molecule. The excitation is assumed to be from the Cl 1s level core. This level has a binding energy of 2822 eV, such that, with the photon energy of 4522 eV used in the previous study, the kinetic energy will be a relatively high 1700 eV. In addition, because of the dipole selection rule in the photoelectric effect, the emitted photoelectrons will be p waves whose intensity maxima are oriented along the linear polarization vector of the incoming light. Thus, there will be a nodal plane perpendicular to this vector, as shown in Fig. 13(a), with non-zero photoelectron intensity directly in this plane only being possible via elastic scattering from other atoms in the molecule. In the previous study, the theoretical simulations considered only three atoms in the cluster, as shown in Fig. 13(a): the emitter chlorine atom at the origin (0, 0, 0), carbon atom 2, and carbon atom 6. We have thus explored the degree to which other scatterers in the molecule may be important in such PH imaging. For example, a very simple argument suggests that a more realistic treatment should include carbon atom 1 because it is closest to the emitter, and for the polarization direction shown also maximally in the lobe of the p wave emitted from Cl. Thus, this carbon atom should scatter photoelectrons more strongly than carbon atoms 2 and 6. In fact, Figs. 13(b) and (c) show the difference between including only two scatterers and the full molecule on the section of the hologram that was used in the prior paper, and the differences are enormous. With two scatterers at 1700 eV, not surprisingly the two forward scatterers with their overlapping interference fringes are clearly seen. But with all scatterers, including the emitter for multiple scattering, the hologram is much more complex. The full hemisphere hologram at 1700 eV with all atoms is shown in Fig. 13(d), with Fig. 13(c) representing the central section of this.

Calculations of the diffraction pattern in the normal detection geometry shown in Fig. 13(a) were carried out over a full hemisphere of detection range using the EDAC online program [39]. The holographic image functions $U\left(\vec{r}\right)$ were derived with software developed by Thevuthasan, Len, et al. [66] which is in turn based on the Barton algorithm of $U\left(\vec{r}\right) = \left| \iiint H\left(\vec{k}\right) \mathrm{e}^{\left[-i\vec{k}\cdot\vec{r}+ikr\right]} d^3k \right|$, with $H\left(\vec{k}\right)$ the usual normalized hologram obtained from $H\left(\hat{k}\right) = (I - I_o)/\sqrt{I_o}$, where I is the intensity with all diffraction effects included, and I_0 is the intensity of Cl 1s with no scatterers present. No corrections for scattering factor amplitudes or phase shifts were made. And no vibrational attenuation was included, through a rigid atom model. Thus, more accurate and realistic images with reduced effects of multiple scattering could no doubt be obtained in the future with allowance for these effects. Two energy regimes were considered, one with a fairly high kinetic energy of 1700 eV, and one with a lower energy of 300 eV, with the latter expected to reduce deleterious forward scattering effects. Specifically, single-energy images at 1700 eV and 300 eV were obtained, and multi-energy

images with 10 energies over 1443–1977 eV and approximately centered on 1700 eV and over 150–478 eV and centered approximately on 300 eV were studied. The effects of multiple scattering up to third order were also investigated.

As expected, the lower energy images were of better quality than those at higher energy due to forward scattering effects [49]. Also, multi-energy images were not surprisingly better than those based on a single energy. We thus only show a sequence of images from single and multiple low-energy holograms in Fig. 14: (a) single energy of 300 eV, (b) multiple low energies with first-order scattering only, (c) multiple low energies up to second-order scattering, and (d) multiple low energies up to third-order scattering. In (a) for a single energy, reasonable imaging in the two relevant high symmetry planes of the molecule is found, but of course with an identical twin image for negative z. Atom C_4, farthest from the emitter, is also rather weak for this case. For multiple energies with single scattering, the imaging is much improved, including atom C_4. Interestingly, multiple energies with both second-order and third-order scattering yield better images, including atom C_4. Using multiple energies is clearly a desirable thing to do, although imaging should be possible to some degree, perhaps in proof of principle experiments, with only a single energy. And to be sure, in all images there are atom-image peak shifts from the ideal geometry, with these being of the order of 0.1–0.3 Å, in the *z* direction [49], but we can nonetheless conclude that it should be possible to follow atomic dynamics, for example, in dissociation after some kind of pump pulse so as to generate true molecular movies. This thus represents another exciting future perspective for photoemission.

7. Concluding remarks

We have thus pointed out several new dimensions of photoemission that are promising for future studies of both condensed phases and free molecules. Specifically, large-angle datasets require more accurate consideration of both atomic differential cross sections and the basic theory of photoemission, particularly for ARPES measurements. Going to higher excitation energies in the multi-keV regime opens up new possibilities for studying bulk electronic structure in complex materials, as well as the buried layers and interfaces that are critical to the properties of many nanoscale systems, e.g. in catalysis, spintronics, photovoltaics and electrochemistry. ARPES has recently been extended into the multi-keV range, thus providing a new tool for studying the bulk electronic structure of complex materials. Standing-wave, total reflection, and resonance effects can also be used in several ways to enhance depth and orbital sensitivity (see also ref. 1), with a novel area of application being in photoemission at high ambient pressure, and the latter promising new insight into the solid/liquid interface. Finally, photoelectron holography from free molecules shows promise in future pump-probe studies of providing the means for taking molecular movies of atomic motion and yielding unprecedented detail of molecular dynamics. We have illustrated these new dimensions with applications to a magnetic semiconductor, multilayer structures of complex metal oxides, a thin water solution on a metal oxide surface, and a halo-substituted benzene molecule.

Acknowledgements

This work has been supported by the Director, Office of Science, Office of Basic Energy Sciences, Materials Sciences and Engineering Division, of the U.S. Department of Energy under Contract No. DE-AC02-05CH11231, through the Materials Sciences Division of the Lawrence Berkeley National Laboratory (LBNL). Additional support has come from Army Research Office MURI grant W911-NF-09-1-0398, in particular for the GTO/STO study; the Jülich Research Center, Peter Grünberg Institute (PGI-6); and from the LABEX-PALM APTCOM Project of the Triangle de Physique (Paris). We are also grateful to various co-authors and staff scientists who have provided excellent assistance with measurements at the Advanced Light Source, SPring-8, the Swiss Light Source, Soleil, and Petra III.

References

[1] A.X. Gray, Future directions in standing-wave photoemission, J. Electron Spectrosc. Rel. Phenom. 195 (2014) 399–408.
[2] H. Matsuda, L. Tóth, F. Matsui, H. Daimon, Evaluation of disturbing effect of mesh holes inwide-acceptance-angle electrostatic mesh lenses, J. Electron Spectrosc. Rel. Phenom. 195 (2014) 78–84.
[3] T. Matsushita, F. Matsui, Features of atomic images reconstructed from photoelectron, Augerelectron and internal detector electron holography using SPEA-MEM, J. Electron Spectrosc. Rel. Phenom. 195 (2014) 365–374.
[4] S. Nemšák, N. Kaduwela, C.S. Fadley, program based on equations from ref. 5, to be published in an open access format.
[5] S. Goldberg, S. Kono, C.S. Fadley, J. Electron Spect. 21 (1985) 285.
[6] J. Braun, Rep. Prog. Phys. 59 (1996) 1267, J. Minár, J., Braun, S., Mankovsky, H., Ebert, Journal of Electron Spectroscopy and Related Phenomena,184, 91 (2011).
[7] M. Salmeron, R. Schlögl, Surf. Sci. Rep. 63 (2008) 169.
[8] D.E. Starr, Z. Liu, M. Hävecker, A. Knop-Gericke, H. Bluhm, Chem. Soc. Rev. 42 (2013) 5833.
[9] S. Tanuma, C.J. Powell, D.R. Penn, Surf. Interf. Anal. 43 (2011) 689.
[10] F. Offi, S. Iacobucci, P. Vilmercati, A. Rizzo, A. Goldoni, M. Sacchi, G. Panaccione, Phys. Rev. B 77, 201101R (2008).
[11] F. Offi, S. Iacobucci, L. Petaccia, S. Gorovikov, P. Vilmercati, A. Rizzo, A. Ruocco, A. Goldoni, G. Stefani, G. Panaccione, J. Phys.: Conden. Matter 22 (2010) 305002.
[12] Nuclear Instruments and Methods A 547, 24-41 (2005), papers from first HXPS conference, J. Zegenhagen, Ed.
[13] Journal of Electron Spectroscopy 178–179, 1-448 (2010), dedicated issue on XPS and HXPS, L., Kover, Ed.; and dedicated issue on HXPS, loc. cit. 190, 125-314 (2013), W. Drube, Ed.
[14] S. Axnanda, E. Crumlin, R. Chang, B.H. Mao, S. Rani, P. Ross, Z. Hussain, Z. Liu, to be published.
[15] T. Matsushita, T. Muro, Y. Saitoh, T. Nakatani, A. Sekiyama, S. Suga, Surf. Rev. Lett. 9 (2002) 1321, and earlier references therein.
[16] A.X. Gray, C. Papp, S. Ueda, B. Balke, Y. Yamashita, L. Plucinski, J. Minár, J. Braun, E.R. Ylvisaker, C.M. Schneider, W.E. Pickett, H. Ebert, K. Kobayashi, C.S. Fadley, Nat. Mater. 10 (2011) 759, accompanying News and Views, D. L. Feng, *Nature Materials* 10, 729-730.
[17] Charles S. Fadley, Synchrotron Radiat. News 25 (2012) 26.
[18] Z. Hussain, C.S. Fadley, S. Kono, L.F. Wagner, Phys. Rev. B 22 (1980) 3750, R. C. White, C. S. Fadley, M. Sagurton, and Z. Hussain, Physical Review B 34, 5226 (1986).
[19] P. Hofmann, C. Sondergaard, S. Agergaard, S.V. Hoffmann, J.E. Gayone, G. Zampieri, S. Lizzit, A. Baraldi, Phys. Rev. B 66 (2002) 245422.
[20] F. Venturini, J. Minar, J. Braun, H. Ebert, N.B. Brookes, Phys. Rev. B 77 (2008) 045126.
[21] L. Plucinski, J. Minár, B.C. Sell, J. Braun, H. Ebert, C.M. Schneider, C.S. Fadley, Phys. Rev. B 78 (2008) 035108;
C. Papp, L. Plucinski, J. Minar, J. Braun, H. Ebert, C.M. Schneider, C.S. Fadley, Phys. Rev. B 84 (2011) 045433.
[22] J. Braun, J. Minar, S. Mankovsky, L. Plucinski, V.N. Strocov, N.B. Brookes, C.M. Schneider, C.S. Fadley, H. Ebert, Phys. Rev. B 88 (2013) 205409.
[23] C.S. Fadley, J. Electron Spectrosc. 190 (2013) 165–179.
[24] S. Nemšák, L. Plucinski, unpublished results from ALS beamline 9.3.1.
[25] B.L. Gyorffy, Phys. Rev. B5 (1973) 2382.
[26] S.-H. Yang, A.X. Gray, A.M. Kaiser, B.S. Mun, J.B. Kortright, C.S. Fadley, J. Appl. Phys. 113 (2013) 073513, http://dx.doi.org/10.1063/1.4790171, A versatile downloadable software package for calculating such effects, the Yang X-Ray Optics (YXRO) program, is also available at: https://sites.google.com/a/lbl.gov/yxro/home.
[27] A.X. Gray, C. Papp, B. Balke, S.-H. Yang, M. Huijben, E. Rotenberg, A. Bostwick, S. Ueda, Y. Yamashita, K. Kobayashi, E.M. Gullikson, J.B. Kortright, F.M.F. de Groot, G. Rijnders, D.H.A. Blank, R. Ramesh, C.S. Fadley, Phys. Rev. B 82 (2010) 205116.
[28] F. Kronast, R. Ovsyannikov, A. Kaiser, C. Wiemann, S.-H. Yang, D.E. Bürgler, R. Schreiber, F. Salmassi, P. Fischer, H.A. Dűrr, C.M. Schneider, W. Eberhardt, C.S. Fadley, Appl. Phys. Lett. 93 (2008) 243116.
[29] S.H. Yang, B. Balke, C. Papp, S. Döring, U. Berges, L. Plucinski, C. Westphal, C.M. Schneider, S.S.P. Parkin, C.S. Fadley, Phys. Rev. B 84 (2011) 184410.
[30] S. Nemšák, G. Conti, A.X. Gray, G. Pálsson, C. Conlon, D. Eiteneer, A. Keqi, A. Rattanachata, A.Y. Saw, A. Bostwick, L. Moreschini, V. Strocov, M. Kobayashi, W. Stolte, A. Gloskovskii, W. Drube, M.-C. Asencio, J. Avila, P. Moetakef, C. Jackson, A. Janotti, C.G. Van de Walle, J. Minar, J. Braun, H. Ebert, L. Plucinski, C.M. Schneider, S. Stemmer, C.S. Fadley, to be published.
[31] J. Chester, T. Jach, S. Thurgate, J. Vac. Sci. Technol. B 11 (1993) 1609, J. Kawai, S., Hayakawa, Y., Kitajima, K. Maeda and Y. Gohshi, J. Electron Spectrosc. Rel. Phenom.
[32] J. Rault, S. Nemšák, G. Pálsson, M. Bibes, C. Conlon, D. Eiteneer, A. Keqi, A. Rattanachata, J.-P. Rueff, C.S. Fadley, to be published.

[33] H. Yamada, M. Marinova, P. Altuntas, A. Crassous, L. Bégon-Lours, S. Fusil, E. Jacquet, V. Garcia, K. Bouzehouane, A. Gloter, J.E. Villegas, A. Barthélémy, M. Bibes, Sci. Repts. 3 (2013) 2834.
[34] B.L. Henke, Phys. Rev. A 6 (1972) 94.
[35] M.J. Bedzyk, G.M. Bommarito, J.S. Schildkraut, Phys. Rev. Lett. 12 (1989) 1376, M.J. Bedzyk, L. Cheng, Reviews in Mineralogy and Geochemistry, 49, 221-266 (2002).
[36] A.X. Gray, J. Minar, S. Ueda, P.R. Stone, Y. Yamashita, J. Fujii, J. Braun, L. Plucinski, C.M. Schneider, G. Panaccione, H. Ebert, O.D. Dubon, K. Kobayashi, C.S. Fadley, Nat. Mater. 11 (2012) 957.
[37] A. Winkelmann, J. Garcia de Abajo, C.S. Fadley, New J. Phys. 10 (2008) 113002.
[38] A. Winkelmann, Influence of localized inelastic scattering on Kikuchi bandsin photoelectron diffraction patterns, J. Electron Spectrosc. Rel. Phenom. 195 (2014) 361–364.
[39] The multiple scattering program EDAC due to J. Garcia de Abajo for calculating photoelectron diffraction is available via Widgets at: http://nanophotonics.csic.es/, with the methodology behind it described in F.J. Garcia de Abajo, M.A. Van Hove, C.S. Fadley, Phys. Rev. B 63, 075404 (2001).
[40] I. Bartos, I. Pıs, M. Kobata, K. Kobayashi, M. Cukr, P. Jiricek, T. Sugiyama, E. Ikenaga, Phys. Rev. B 83 (2011) 235327.
[41] A.X. Gray, J. Minár, L. Plucinski, M. Huijben, A. Bostwick, E. Rotenberg, S.-H. Yang, J. Braun, A. Winkelmann, D. Eiteneer, A. Rattanachata, A. Greer, G. Rijnders, D.H.A. Blank, D. Doennig, R. Pentcheva, J.B. Kortright, C.M. Schneider, H. Ebert, C.S. Fadley, Letters 104 (2013) 17004.
[42] S. Nemšák, A.X. Gray, S. Döring, G. Conti, C. Conlon, J. Minár, L. Plucinski, M. Huijben, S.-H. Yang, J. Braun, G. Rijnders, D.H.A. Blank, M. Kobayashi, V. Strocov, J.B. Kortright, C.M. Schneider, H. Ebert, C.S. Fadley, to be published.
[43] P. Moetakef, J.Y. Zhang, A. Kozhanov, B. Jalan, R. Seshadri, S.J. Allen, S. Stemmer, Appl. Phys. Lett. 98 (2011) 232116, P. Moetakef, T.A., Cain, D.G., Ouellette, J.Y., Zhang, D.O., Klenov, A., Janotti, C.G. Van de Walle, S., Rajan, S.J., Allen, S., Stemmer, Applied Physics Letters 99, 232116 (2011); C. Jackson, P., Moetakef, S.J., Allen, S., Stemmer, Applied Physics Letters 100, 232106 (2012); P. Moetakef, J.R., Williams, D. G. Ouellette, A.P., Kajdos, D. Goldhaber-Gordon, S.J., Allen, S., Stemmer, Phys. Rev. X 2, 021014 (2012).
[44] W. Meevasana, P.D.C. King, R.H. He, S-K. Mo, M. Hashimoto, A. Tamai, P. Songsiriritthigul, F. Baumberger, Z-X. Shen, Nat. Mater. 10 (2011) 114.
[45] S. Nemšák, A. Shavorskiy, O. Karslioglu, I. Zegkinoglou, A. Rattanachata, C.S. Conlon, A. Keqi, P.K. Greene, K. Liu, F. Salmassi, E.M. Gullikson, H. Bluhm, C.S. Fadley, to be published.
[46] Electrochemical Aspects of Ionic Liquids, H. Ohno (John Wiley & Sons, 2011).
[47] Mineral-Aqueous Solution Interfaces and Their Impact on the Environment, G.E. Brown and G. Calas, Geochemical Perspectives 1, 483–742, with special discussion of the mineral-electrolyte double layer over pp. 552–557.
[48] W. Smekal, W.S.M. Werner, C.J. Powell, Surf. Interface Anal. 3 (2005) 1059, W.S.M. Werner, W. Smekal, T. Hisch, J. Himmelsbach, C.J. Powell, J. Electron Spectrosc. 190, 137 (2013).
[49] X.-L. Sun, A.P. Kaduwela, A.X. Gray, C.S. Fadley, Phys. Rev. A 89 (2014) 053415.
[50] A. Szöke, in Short Wavelength Coherent Radiation: Generation and Applications, AIP Conf. Proc. No. 147, edited by D. T. Attwood and J. Boker (AIP, New York, 1986), p. 361.
[51] J.J. Barton, Phys. Rev. Lett. 61 (1988) 1356.
[52] J.J. Barton, Phys. Rev. Lett. 67 (1991) 3106.
[53] B.P. Tonner, Z.-L. Han, G.R. Harp, D.K. Saldin, Phys. Rev. B (14) (1991) 423.
[54] A. Stuck, D. Naumovicí, T. Greber, J. Osterwalder, L. Schlapbach, Surf. Sci. 274 (1992) 441.
[55] C.S. Fadley, Surf. Sci. Rep. 19 (1993) 231.
[56] J. Osterwalder, R. Fasel, A. Stuck, P. Aebi, L. Schlapbach, J. Electron Spectrosc. Relat. Phenom. 68 (1994) 1.
[57] P.M. Len, J.D. Denlinger, E. Rotenberg, S.D. Kevan, B.P. Tonner, Y. Chen, M.A. Van Hove, C.S. Fadley, Phys. Rev. B 59 (1999) 5857.
[58] C.S. Fadley, M.A. Van Hove, A. Kaduwela, S. Omori, L. Zhao, S. Marchesini, J. Phys. Cond. Mat. 13 (2001) 10517.
[59] T. Matsushita, F. Matsui, H. Daimon, K. Hayashi, J. Electron Spectrosc. Rel. Phenom. 178 (2010) 195.
[60] C.S. Fadley, J. Electron Spectrosc. Rel. Phenom. 178 (2010) 2.
[61] T. Greber, J. Phys. Cond. Mat. 13 (2001) 10561.
[62] A. Landers, Th. Weber, I. Ali, A. Cassimi, M. Hattass, O. Jagutzki, A. Nauert, T. Osipov, A. Staudte, M.H. Prior, H. Schmidt-Böcking, C.L. Cocke, R. Dörner, Phys. Rev. Lett. 87 (2001) 013002.
[63] Th. Weber, O. Jagutzki, M. Hattass, A. Staudte, A. Nauert, L. Schmidt, M.H. Prior, A.L. Landers, A. Brauning-Demian, H. Brauning, C.L. Cocke, T. Osipov, I. Ali, R. Diez-Muino, D. Rolles, F.J. Garcia de Abajo, C.S. Fadley, M.A. Van Hove, A. Cassimi, H. Schmidt-Bocking, R. Dorner, J. Phys. B, At. Mol. Opt. Phys. 34 (2001) 3669.
[64] R. Diez-Muino, D. Rolles, F.J. García de Abajo, C.S. Fadley, M.A. Van Hove, Surf. Rev. Lett. 9 (2002) 1213.
[65] F. Krasniqi, B. Najjari, L. Struder, D. Rolles, A. Voitkiv, J. Ullrich, Phys. Rev. A 81 (2010) 033411.
[66] P.M. Len, PhD Thesis, June 1997, University of California–Davis, available at: http://www.osti.gov/bridge/servlets/purl/539829-N9C147/webviewable/539829.pdf; P.M. Len, S. Thevuthasan, C.S. Fadley, A.P. Kaduwela, M.A. Van Hove, Phys. Rev. B 50, 11275 (1994).